

Electronic Supplementary Information

Designing Chemically Selective Liquid Crystalline Materials that Respond to Oxidizing Gases

Nanqi Bao,^{†,a} Jake I. Gold,^{†,b} Tibor Szilvási,^b Huaizhe Yu,^a Robert J. Twieg,^c Manos Mavrikakis,^{*,b} and Nicholas L. Abbott^{*,a}

Additional Computational Details

1. Additional binding energy calculations

We calculated reaction free energies for formation of bulk metal-perchlorate salts, metal-oxide, and metal-oxyhydroxide structures as follows: Crystal structures for $\text{Co}(\text{ClO}_4)_2$ and $\text{Ni}(\text{ClO}_4)_2$ have been reported to have the same octahedral geometry with lattice constants of $a = 4.83 \text{ \AA}$, $c = 21.70 \text{ \AA}$ and $a = 4.77 \text{ \AA}$, $c = 21.85 \text{ \AA}$, respectively.¹ This is in close agreement to our DFT optimized lattice constants for $\text{Co}(\text{ClO}_4)_2$ and $\text{Ni}(\text{ClO}_4)_2$ of $a = 4.95 \text{ \AA}$, $c = 22.08 \text{ \AA}$ and $a = 4.77 \text{ \AA}$, $c = 21.72 \text{ \AA}$, respectively. We could not find a representative structure for $\text{Mn}(\text{ClO}_4)_2$ in the literature; therefore, we used the same structure as the one reported for $\text{Co}(\text{ClO}_4)_2$ and $\text{Ni}(\text{ClO}_4)_2$ ¹ and found the optimal lattice constants to be $a = 5.00 \text{ \AA}$, $c = 22.28 \text{ \AA}$. In order to calculate the bulk formation free energies, we reference the oxidized Mn salt structures to rutile $\beta\text{-MnO}_2$ with DFT calculated lattice constants of $a = 4.46 \text{ \AA}$, $c = 2.94 \text{ \AA}$, which is in close agreement to literature reported values of $a = 4.39$, $c = 2.87$.² We model $\beta\text{-MnO}_2$ because it is the most thermodynamically stable crystal structure of MnO_2 . We referenced the formation free energies of oxidized Ni and Co structures to $\beta\text{-NiOOH}$, and CoOOH , for which the DFT-calculated lattice constants were $a = 5.26 \text{ \AA}$, $b = 2.81 \text{ \AA}$, $c = 9.10 \text{ \AA}$ and $a = b = c = 4.64 \text{ \AA}$, respectively. These are also in relatively good agreement with reported values for $\beta\text{-NiOOH}$ ($a = 4.88 \text{ \AA}$, $b = 2.92 \text{ \AA}$, $c = 9.24 \text{ \AA}$)³ and the Inorganic Crystal Structure Database (ICSD) value for CoOOH ($a = b = c = 4.69 \text{ \AA}$)⁴.

We constructed surfaces based on the bulk relaxed structures described above. We selected the most stable rutile phase of MnO_2 ($\beta\text{-MnO}_2$) with the most stable (110) facet as the most likely structure to form after oxidation of the perchlorate salt. For $\beta\text{-MnO}_2$, we used a (4x2) slab with four MnO_2 trilayers, of which the bottom two were fixed at the calculated bulk atomic positions. Because the oxidation requires water, we hydroxylated the pristine $\beta\text{-MnO}_2$ slab as done in a previously reported structure.⁵ CoOOH and NiOOH form layered structures similar to what has been reported for graphene or $\alpha\text{-PtO}_2$ in which layers interact weakly with mostly Van der Waals interactions or hydrogen bonds for the case of CoOOH and NiOOH . Therefore, we assume the most stable facet is one where we cut the slab in between these layers, which corresponds to the (0001) facet. We used a (4x2) unit cell slab that contains three layers with the bottom two layers fixed to the calculated bulk constants for both CoOOH and NiOOH . For all slab models, 20 \AA of vacuum separated the pristine slabs. Dipole corrections were applied in the direction normal to the surface⁶.

We used the neutral anion model (NAM) to calculate binding energies and binding free energies to metal perchlorate structures. Details of this model can be found elsewhere⁷⁻⁹, but we briefly summarize the most important features of this model here. The NAM is a cluster model that contains one cation and sufficient anions to make the overall charge neutral. This means that the NAM is stoichiometrically consistent with the metal salts used in experiments. We have previously shown that this model correctly predicted displacement for 9 out of 10 cases when compared to experiment.⁷⁻¹⁰

Gibbs free energies were calculated using the harmonic approximation. The mass-weighted Hessian was built up via numerical differentiation of the energy using a second-order finite difference approach with a step size of 0.008 \AA . Vibrational analysis was used to calculate entropies and enthalpies at 300 K. Gibbs free binding energies were calculated as:

$$G_{BE} = G_{tot} - G_{gas} - G_{clean}$$

where G_{tot} is the total free energy of the slab with the adsorbate on the surface, G_{gas} is the total free energy of the gas-phase adsorbate, and G_{clean} is the total free energy of the clean slab. All binding free energies are calculated at the limit of low coverage with one adsorbate per slab or cluster. We assume that there is no strong vibrational coupling between the adsorbate and surface, thus slab atoms can be fixed during the vibrational calculations (i.e., we assume that $G_{clean} = E_{clean}$). Bulk formation energies were calculated using the same level of theory as the surface calculations, except that harmonic vibrational frequencies were calculated for all bulk atoms.

Table S1. Calculated binding free energy (G_{BE} in eV) of PhCN, the surrogate of 5CB, to metal cations with low oxidation states (LOS) as perchlorate salts (2+ cations) and high oxidation states (HOS) in the form of oxyhydroxides (3+ cations) and oxide (4+ cation) surfaces. For the HOS state, we report PhCN binding in both parallel and perpendicular orientations

Cation (LOS/HOS)	LOS G_{BE} (eV)	HOS G_{BE} Parallel (eV)	HOS G_{BE} Perpendicular (eV)
Mn (2+/4+)	-0.43	+0.12	+0.69
Co (2+/3+)	-0.48	-0.25	+0.37
Ni (2+/3+)	-0.52	-0.22	+0.43

^aFor the HOS calculations on an extended surface, we report both parallel and perpendicular states. Parallel binding is preferred for all cases due to weak perpendicular binding free energies. Because NAM is a cluster model, we only report one G_{BE} value, which corresponds to the nitrile-metal cation interaction.

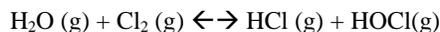
The influence of dispersion corrections (Grimme's D3) on the binding energy for PhCN to the low oxidation state (LOS) in perpendicular alignment and the high oxidation state (HOS) in parallel alignment is summarized in Table S2. We observed that dispersion corrections contribute only a small portion of the overall binding energy for the LOS in perpendicular alignment (< 0.15 eV). This is due to the molecule interacting primarily through one atom (nitrogen) with the surface. In contrast, dispersion corrections contribute much more to the binding energy calculated for parallel alignment on the HOS surfaces. In parallel alignment, all atoms in PhCN interact with the surface, which makes dispersion interaction much more prevalent.

Table S2. Calculated binding energies (eV) without (with) dispersion corrections for PhCN, the surrogate of 5CB, to metal cations in the low oxidation state (LOS) form of perchlorate salt (2+ cations) and the high oxidation state (HOS) form of oxyhydroxides for 3+ cations and oxide for 4+ cation. Value outside the parentheses is without dispersion corrections; Value inside the parentheses is with dispersion corrections included, using the same geometry (single point calculation). For the HOS states, entries correspond to parallel orientation, whereas for LOS states, entries correspond to perpendicular orientation.

Cation (LOS/HOS)	LOS BE (eV)	HOS BE (eV)
Mn (2+/4+)	-0.98 (-1.11)	-0.09 (-0.67)
Co (2+/3+)	-0.95 (-1.09)	-0.30 (-0.93)
Ni (2+/3+)	-1.12 (-1.24)	-0.24 (-0.89)

2. Calculation of formation energies

To calculate formation energies, we used the reactions shown in Equations 3 – 14 in the main manuscript. Because these equations have gas phase species (Cl_2 , O_3 , O_2 , H_2O , HCl , $HClO_4$), in order to calculate formation free energies, we must include pressure corrections by assuming all surface species are in equilibrium with the gas phase species. The pressures of some of these gas phase species are set by the experimental conditions such as Cl_2 (1 – 8 ppm), O_3 (0.3 – 1290 ppm), O_2 (0.2 atm in air), and H_2O (4,912 ppm at 20% RH). However, there are other gas phase pressures that are unknown during experimental conditions such as HCl , NO , and $HClO_4$. To obtain an order-of-magnitude estimate of these pressures, we must make some additional assumptions. We assume that the following reaction is in equilibrium to form HCl from Cl_2 and H_2O :¹¹



It has been proposed that the above reaction is the mechanism by which Cl_2 can oxidize Mn^{2+} by first forming $HOCl (g)$.¹² If we assume this reaction is in equilibrium and $P_{HCl} = P_{HOCl}$ (based on a 1:1 stoichiometric coefficients in this reaction), then we can use this equation to solve for the pressure of HCl to define the chemical potential of this species. We note that because Equations 6-8 in the main manuscript for Cl_2 -based oxidation have different HCl coefficients; assumptions on the chemical potential of these species are important and can change the relative order of the formation free energy calculations in Table 1.

For the NO pressure estimation, we made assumptions similar to the case of HCl , and assume that the following reaction is in equilibrium:



The above reaction has been shown to occur at temperatures as low as 86 K at the interface of the condensed phase of NO₂ and H₂O.¹³ Because the pressures of O₂ and NO₂ are known from experimental conditions, we can calculate the pressure of NO from this equation.

To estimate the chemical potential of HClO₄, we had to make additional assumptions. For each reaction studied, one mole of HClO₄ is produced per mole of metal cation oxidized. Because HClO₄ is neutral and we expect the surface to be fully hydroxylated, HClO₄ can only interact with the surface via van der Waals interactions or hydrogen bonding. Due to these weak interactions with the surface, HClO₄ will remain dissolved in the LC solution. Therefore, the chemical potential of HClO₄ can be approximated by the chemical potential of HClO₄ in the LC solution, which should be approximately the same for all systems studied. We note that because Equations 3-14 all have the same HClO₄ stoichiometric coefficients (1 mole HClO₄ produced per mole of cation oxidized), our approximation for the value of the chemical potential of HClO₄ does not influence the relative order of reaction free energies used to determine the cations that are most thermodynamically favored to be oxidized. Therefore, even if our chemical potential estimate of HClO₄ is inaccurate, our interpretation on the relative order of stability would be the same. We assumed the gas phase species are in equilibrium with the LC solution by the Henry's Law constant, H. The value for constant H for HClO₄ at the air-water interface is 9.9 x 10³ mol/m³/Pa.¹⁴ The Henry's law coefficient for partitioning into the LC generally falls in the same order of magnitude for water and toluene.¹⁵ Thus, we assume the air-water Henry's law coefficient as an approximate value for our air-LC systems. Using these assumptions, we can define the pressure of HClO₄ by using the equation below (S1).

$$P_{HClO_4} = C_{HClO_4} H_{HClO_4} \quad S1$$

In equation S1, we still need to specify the concentration of the product HClO₄ in the LC. We know that the initial concentration of HClO₄ is zero and increases to the concentration determined by the final oxidized state (assumed to be ~1 ML for these calculations). We averaged these two quantities and assumed the HClO₄ concentration to correspond to 0.5 ML of oxidized metal salt. We can determine the molar density of cations oxidized at ½ ML to be $\frac{1}{2} S_A$ where S_A is the molar surface density of metal cations for the perchlorate salts. Therefore, the concentration of HClO₄ is determined in Equation S2.

$$C_{HClO_4} = \frac{\frac{1}{2} S_A \nu}{\delta_{LC}} \quad S2$$

where ν is the stoichiometric coefficient that relates HCl or HClO₄ to the molar metal cation density determined by Equations 3-8 in the main manuscript. The term δ_{LC} is the liquid crystal thickness (18 μm). Finally, we can combine Equation S1 and S2 to obtain the pressure relationship in S3.

$$P_{HClO_4} = \frac{\frac{1}{2} S_A \nu H_{HClO_4}}{\delta_{LC}} \quad S3$$

The S_A values used in S3 were determined using the (001) facet of the relaxed bulk structures. For Ni(ClO₄)₂, Co(ClO₄)₂, and Mn(ClO₄)₂, S_A is 8.42x10⁻¹⁰ mol/cm², 7.83x10⁻¹⁰ mol/cm², and 7.68x10⁻¹⁰ mol/cm², respectively. These values vary slightly for each metal cation based on the small differences in the first principles calculated lattice constants.

Table S3. DFT calculated reaction energies (ΔE), reaction standard free energies at 1 atm (ΔG°), and reaction free energies at relevant experimental pressures (ΔG) for Equations 3-14.^a

Analyte	Cation	ΔE (eV)	ΔG° (eV)	ΔG (eV)
O ₃	Mn ²⁺	-0.25	-0.39	-1.24
O ₃	Ni ²⁺	0.03	0.13	-0.71
O ₃	Co ²⁺	0.02	0.17	-0.67
Cl ₂	Ni ²⁺	1.00	1.12	-0.15
Cl ₂	Mn ²⁺	1.71	1.60	-0.11
Cl ₂	Co ²⁺	1.00	1.17	-0.10
O ₂	Ni ²⁺	0.67	0.89	-0.01
O ₂	Co ²⁺	0.67	0.94	0.04
O ₂	Mn ²⁺	1.03	1.13	0.17
NO ₂	Ni ²⁺	1.25	1.37	0.40
NO ₂	Co ²⁺	1.24	1.42	0.45
NO ₂	Mn ²⁺	2.18	2.10	1.13

^aReaction energies are ordered according to a decreasing thermodynamic driving force using the ΔG value. Free energies are calculated at 300 K. For ΔG calculations, we use the experimentally relevant gas phase pressures: 0.21 atm O₂, 20% relative

humidity (RH) H₂O (4,912 ppm), 1290 ppm O₃, 8 ppm Cl₂, and 8 ppm NO₂. For estimates of the pressure of HCl, NO, HClO₄, see above.

We also compare the influence of dispersion correction method on a couple of key results. We compare Grimme's D3 to Grimme's D2 in the section below. We find that the lattice constants for β -MnO₂ with Grimme's D3 ($a = 4.46 \text{ \AA}$, $c = 2.94 \text{ \AA}$) are similar to the values determined with Grimme's D2 ($a = 4.42 \text{ \AA}$, $c = 2.96 \text{ \AA}$), which are both close to the experimentally reported values of $a = 4.39$, $c = 2.87$.² Using the lattice constants for the respective methods, we compare BE in parallel and perpendicular alignment of PhCN on β -MnO₂ in Table S4. We find that the two methods give BEs within 0.05 eV. Therefore, we conclude that the specific dispersion correction method used in the calculations does not play a major role in determining the results presented in this manuscript.

Table S4. Calculated binding energies (eV) for PhCN, the surrogate of 5CB, to MnO₂ surface to compare Grimme's D2 and Grimme's D3 in parallel and perpendicular alignment.

Method	BE Parallel (eV)	BE Perpendicular (eV)
PBE-D2	-0.68	+0.24
PBE-D3	-0.67	+0.20

Additional Experimental Details

1. Materials

Manganese(II) perchlorate hydrate, cobalt(II) perchlorate hexahydrate, nickel(II) perchlorate hexahydrate, aluminum(III) perchlorate nonahydrate salts and potassium iodide were purchased from Sigma-Aldrich (Milwaukee, WI). Fischer's Finest glass slides and starch indicator 1% for iodometric titration were purchased from Fischer Scientific (Pittsburgh, PA). Absolute ethanol (anhydrous, 200 proof) was purchased from Pharmco-AAPER (Brookfield, CT). All chemicals and solvents were of analytical reagent grade and were used as received without any further purification. Deionized water possessed a resistivity of at least 18.2 M Ω cm or greater. 5CB was purchased from Jiangsu Hecheng Advanced Materials Co., Ltd (Jiangsu, China). Cl₂ in nitrogen gas (purity of Cl₂ is 99.9% and purity of nitrogen is 99.998%) at a concentration of 10 ppm and nitrogen gas (99.998% purity) were obtained from Airgas (Elmira, NY) and used as received. Ozone gas was generated using an ozone generator (A2Z Ozone Inc., Louisville, KY). Sodium thiosulfate was purchased from MilliporeSigma (Burlington, MA) for iodometric titration.

2. O₃ gas generation

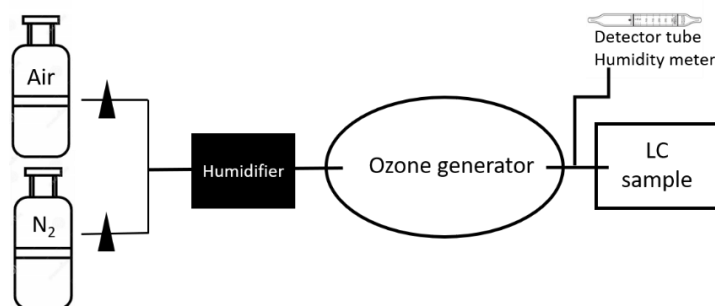


Figure S1. Schematic illustration of the experimental set-up used to expose a supported LC film to an O₃ stream at a desired concentration and relative humidity (RH).

O₃ concentration was controlled by changing the ratio of N₂ and O₂ in the gas source that was delivered to the ozone generator. When using compressed air (80% N₂ and 20% O₂), the ozone generator generated O₃ at a concentration of 1290 \pm 40 ppm, which was determined by using iodometric titration, as described in prior publications^{16,17}. For the generation of O₃ with lower concentrations (100 \pm 10, 4 \pm 1, 1.5 \pm 0.2 ppm), air was mixed with N₂ and then fed to the ozone generator. The desired relative humidity was achieved by using a portable dew point generator (LI-610, LI-COR Biosciences, Lincoln, NE). The

relative humidity in the generated O₃ gas was measured using a humidity meter, and O₃ concentration (lower than 100 ppm) was measured using an O₃ detector tube (Dräger gas detector tubes, Lübeck, Germany) at the outlet of the ozone generator.

3. Characterization of orientations of LCs in optical cells during gas exposure

LC samples hosted within TEM grids supported on metal-salt surfaces were exposed to a stream of nitrogen containing Cl₂ or air containing O₃ within a flow cell that was constructed to direct the gaseous flow across the LC samples while permitting observation using a polarized-light microscope (CH40, Olympus, Melville, NY). A detailed description of the flow cell can be found in a prior publication.¹⁸ The stream of gas containing Cl₂ was obtained from a certified cylinder containing 10 ppm Cl₂ in nitrogen, and diluted with N₂ to the desired concentrations (8±0.3, 5±0.2, and 2±0.1 ppm). The relative humidity (RH) of the N₂ was controlled using a dew point generator. The O₃ stream was generated using an O₃ generator (see details above). The gas fed to the flow cell was maintained at room temperature (approximately 23°C). The flow rate of each gas stream was controlled using a rotameter (Aalborg Instruments and Control, Orangeburg, NY). The total flow rate was maintained at 600 mL/min at atmospheric pressure.

4. 5CB anchoring on humid O₃-exposed Mn²⁺ and Co²⁺-decorated surfaces

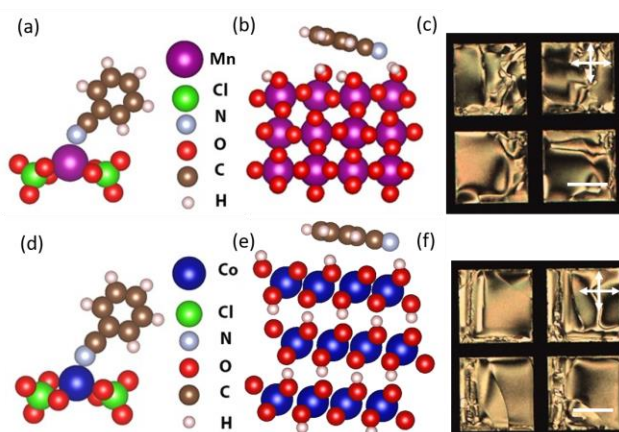


Figure S2. (a) Computed structures used to predict the orientation of 5CB on (a) a Mn²⁺ perchlorate-decorated surface bound to PhCN (24 atoms total, including 11 atoms in the cluster), (b) a hydroxylated MnO₂ surface (Mn⁴⁺) (229 atoms total, including 216 atoms in the slab). (d) a Co²⁺ perchlorate-decorated surface (24 atoms total, including 11 atoms in the cluster), (e) a CoOOH surface (Co³⁺) (205 atoms total including 192 atoms in the slab). (c and f) Optical images (crossed polarizers) of 5CB in a copper grid supported on surfaces decorated with 15±3 pmol/mm² Mn(ClO₄)₂ in (c) and 16±3 pmol/mm² Co(ClO₄)₂ in (f) after exposure to 1290±40 ppm O₃ (5 min at 20% RH) prior to contact with the 5CB. The scale bar is 200 μm.

5. Retardance measurements of 5CB to determine tilt angle of LC

Fiber spacers with 10 μm-diameters (EM Industries, Inc., Hawthorne, NY) were dispersed into Norland Optical Adhesive 65 (Norland Products, Inc., Cranbury, NJ). The perimeters of two metal-salt-decorated glass surfaces were coated with the adhesive, and the surfaces were adhered by UV exposure for 30 minutes. The actual thickness of the cavity between the two glass surfaces was measured by a UV-vis spectrophotometer (Cary 100 UV-vis, Agilent, Santa Clara, CA) based on the interference effect of light.¹⁹ The thickness (*d*) was obtained using the following equation:

$$d = \frac{m}{2\sqrt{n^2 - \sin^2\theta}} \cdot \frac{1}{1/\lambda_1 - 1/\lambda_2}$$

where *d* = film thickness

m = number of complete waves over the wavelength range

n = reflective index of the film material

θ = angle of incidence

*λ*₁ = short wavelength limit

λ_2 = long wavelength limit

We measured the thickness of the gap between two glass surfaces in air, so $n = 1$. In addition, $\theta = 0^\circ$ because the light was incident on the optical cell at normal incidence. λ_1 and λ_2 are picked either from peaks or valleys in the interferogram. The measured thickness of air gap was determined to be $9.7 \pm 0.5 \mu\text{m}$.

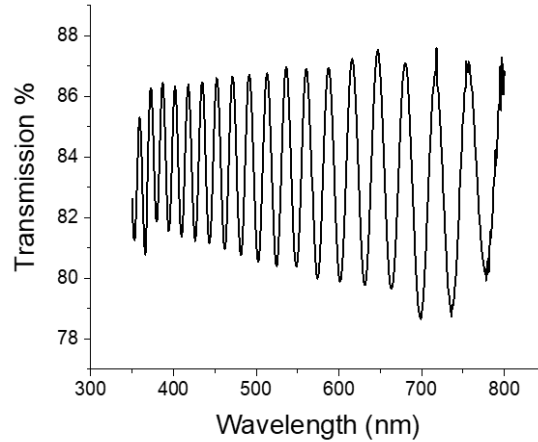


Figure S3. Interferogram obtained using two glass surfaces separated by fiber spacers with $10 \mu\text{m}$ -diameters.

A drop of 5CB, heated to its isotropic phase ($35.5^\circ\text{C} < T < 45^\circ\text{C}$), was then drawn by capillarity into the cavity between the two surfaces of the optical cell. The cell was subsequently cooled to room temperature. The retardance of the LC in Figure S4 was measured using a PolScope (Polaviz, Chagrin Falls, OH), and the value of the tilt angle of 5CB was determined from the known birefringence of 5CB.²⁰ The average LC orientation (white dashed line in Figure S4) indicates that LC mesogens align along the LC flow direction (right to left). The color indicates homogeneity of the LC retardance. The average measured retardance was $1687 \pm 10 \text{ nm}$. The average tilted angle was calculated using the following equation²⁰:

$$\Delta n_{eff} = \frac{n_o n_e}{\sqrt{n_e^2 \sin^2(\theta) + n_o^2 \cos^2(\theta)}} - n_e$$

$$\Delta n_{eff} = \Gamma/d$$

where Δn_{eff} = effective birefringence

n_o = indices of refraction parallel (ordinary refractive index) to the optical axis of the LC

n_e = indices of refraction perpendicular (extraordinary refractive index) to the optical axis of the LC

θ = tilted angle of liquid crystal relative to the surface normal

Γ = retardance of LC film

d = thickness of LC film

The calculated tilt angle of LC, relative to the surface normal, was determined to be $89 \pm 4^\circ$, for 5CB on humid O_3 -exposed $\text{Ni}(\text{ClO}_4)_2$ surfaces.

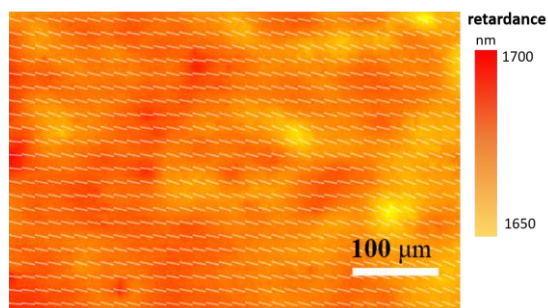


Figure S4. PolScope textures of 5CB sandwiched by two humid O_3 -exposed 15 ± 2 pmol/mm² $Ni(ClO_4)_2$ -decorated glass surfaces. The average LC orientation was indicated by white dashed line. The surfaces were exposed to 1290 ± 40 ppm O_3 (5 min at 20% RH). The scale bar is 100 μm .

6. Orientation of LC on $Al(ClO_4)_3$ -decorated surfaces

We found that 5CB adopted a homeotropic orientation on $Al(ClO_4)_3$ with 16 ± 3 pmol/mm² surface density (Figure S5a). To examine the orientation of 5CB on humid O_3 -exposed $Al(ClO_4)_3$ surfaces, we deposited $Al(ClO_4)_3$ at 16 ± 3 pmol/mm² and then exposed the surface to O_3 gas with 20% RH humidity for 30 minutes. After the exposure, 5CB was deposited on the surface. The LC exhibited a perpendicular orientation (Figure S5b).

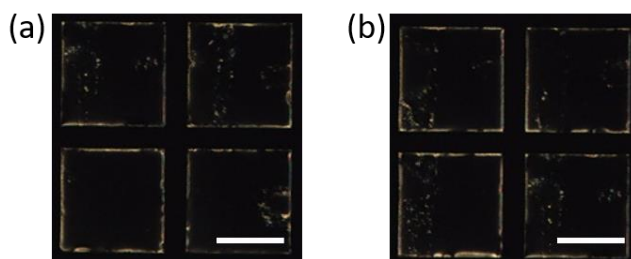


Figure S5. (a) Optical image (crossed polarizers) of 5CB hosted in a copper grid (lateral size of grid square is 285 μm) on a surface decorated with 16 ± 3 pmol/mm² $Al(ClO_4)_3$. (b) Optical image (crossed polarizers) of 5CB in a copper grid supported on an humid O_3 -exposed surface decorated with 16 ± 3 pmol/mm² $Al(ClO_4)_3$ (1290 ± 40 ppm O_3 at 20% RH for 30 min). The scale bar is 200 μm .

7. LC response to dry O_3 , humid O_3 or humid N_2

Water plays an important role in the redox reactions shown in Equations 3-5 of main text. Figure S6 shows 5CB on surfaces of $Mn(ClO_4)_2$, $Co(ClO_4)_2$ or $Ni(ClO_4)_2$, before and after treatment with dry O_3 . To obtain dry O_3 (<0.2% RH), the gas fed to the ozone generator was taken from a gas cylinder (<0.1% RH). We observed that 5CB had no response to dry O_3 on these surfaces, indicating water is needed for the oxidation reactions. Additionally, we observed that 5CB did not respond to 20% RH N_2 gas in 1 hour (Figure S6).

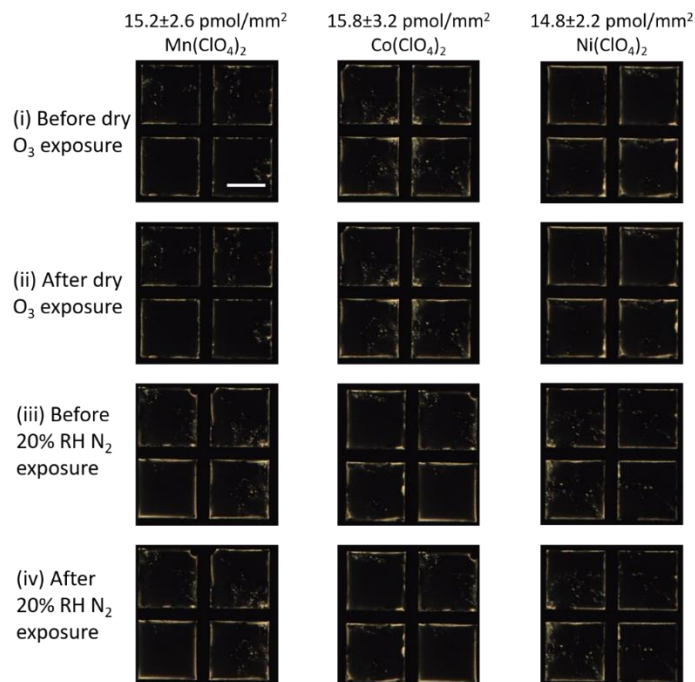


Figure S6. Optical images (crossed polarizers) of 5CB hosted in copper grids (lateral size of grid square is 285 μm) on surfaces decorated with 15 ± 3 pmol/ mm^2 $\text{Mn}(\text{ClO}_4)_2$, 16 ± 3 pmol/ mm^2 $\text{Co}(\text{ClO}_4)_2$, or 15 ± 2 pmol/ mm^2 $\text{Ni}(\text{ClO}_4)_2$ (i) before and (ii) after exposure to 1290 ± 40 ppm dry O_3 (<0.2% RH) for 5 minutes, and (iii) before and (iv) after exposure to 20% RH N_2 for 1 hour. The scale bar is 200 μm .

Table S5. Response time of 5CB on surfaces decorated with 15 ± 3 pmol/ mm^2 $\text{Mn}(\text{ClO}_4)_2$ to 4 ± 1 ppm O_3 with 10%, 20% and 60% RH.

Relative humidity (RH)	10%	20%	60%
Response time (s)	48 ± 7	43 ± 5	42 ± 5

8. XRD of humid O_3 or Cl_2 -exposed surfaces

In the main text, we described the XRD of humid O_3 -exposed $\text{Mn}(\text{ClO}_4)_2$ salt. In addition to new diffraction peaks characteristic of MnO_2 (Figure 4a), the XRD pattern shows evidence of coexistence of MnO_2 and $\text{Mn}(\text{ClO}_4)_2$. This suggests that not all bulk $\text{Mn}(\text{ClO}_4)_2$ salt was oxidized by ozone during the 3-hour exposure. For $\text{Co}(\text{ClO}_4)_2$ after humid O_3 exposure, XRD peaks corresponding to (003), (012) and (017) in CoOOH are evident in Figure 4b, and similar XRD patterns were reported previously for oxidized $\text{Co}(\text{OH})_2$ ^{21,22,23} and nanocrystalline CoOOH .^{24,25} For $\text{Ni}(\text{ClO}_4)_2$ after humid O_3 exposure, the XRD pattern in Figure 4c indicates NiOOH formation ((003), (006), and (108)), which agrees with those reported for NiOOH formed by electrolytic and thermal oxidation of $\text{Ni}(\text{OH})_2$.^{26–29} We also observed the existence of $\text{Co}(\text{ClO}_4)_2$ and $\text{Ni}(\text{ClO}_4)_2$ in the diffraction patterns, (peaks at 31.6° in Figure 4b, and 23.0° in Figure 4c). This result suggests 3 hr-humid O_3 exposure is not sufficient to oxidize all metal salts.

We also characterized bulk $\text{Mn}(\text{ClO}_4)_2$, $\text{Co}(\text{ClO}_4)_2$, and $\text{Ni}(\text{ClO}_4)_2$ salts before and after humid Cl_2 exposure using XRD (Figure S7). The results show that there is no obvious change in crystal structure for bulk $\text{Ni}(\text{ClO}_4)_2$ and $\text{Co}(\text{ClO}_4)_2$ salts after humid Cl_2 exposure (Figure S7b and c). For humid Cl_2 -exposed $\text{Mn}(\text{ClO}_4)_2$, the XRD pattern is similar to that of humid O_3 -exposed $\text{Mn}(\text{ClO}_4)_2$ salt indicating the formation of MnO_2 (Figure 4a and Figure S7a).

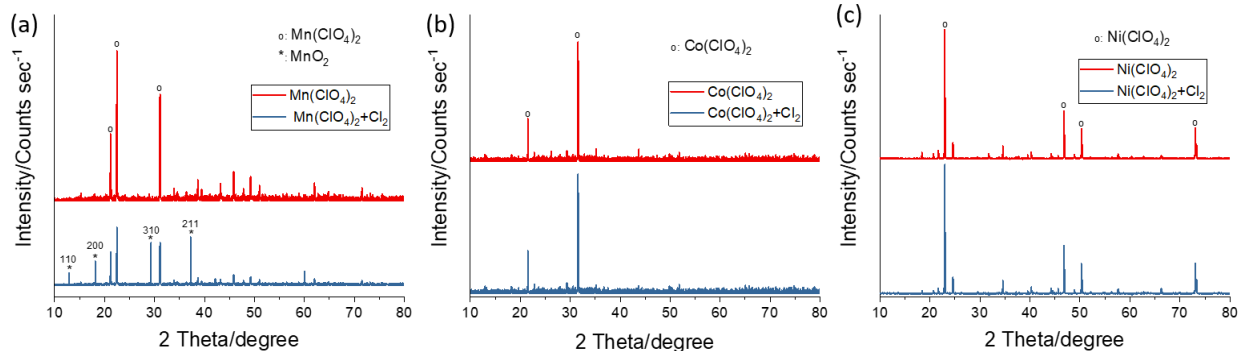


Figure S7. X-ray diffraction patterns of (a) $\text{Mn}(\text{ClO}_4)_2$, (b) $\text{Co}(\text{ClO}_4)_2$, and (c) $\text{Ni}(\text{ClO}_4)_2$ before (in red) and after 12-hour exposure to 8 ppm Cl_2 with 20% RH (in blue). The characteristic peaks for metal perchlorates are indicated with circles, and the characteristic peaks for MnO_2 are labeled by asterisks.

Additional Description of the Reaction-Diffusion Model

1. Derivation of the Transport Model

We previously developed a transport model which assumed that the analyte in the LC film was in equilibrium with the analyte adsorbed at the solid surface ($C_{\text{surf,LC}}$).¹⁸ The model captured the dynamics of DMMP on $\text{Al}(\text{ClO}_4)_3$ (concentration profile visualized in Figure S8a). In addition, the rate limiting process was determined to be diffusion of DMMP to the air side of the LC-interface (concentration $C_{i,\text{Air}}$) from infinitely far away (concentration $C_{\infty,\text{Air}}$). This assumption produces a relatively flat concentration profile of the analyte in the LC ($C_{i,\text{LC}}$) as depicted in Figure S8a.

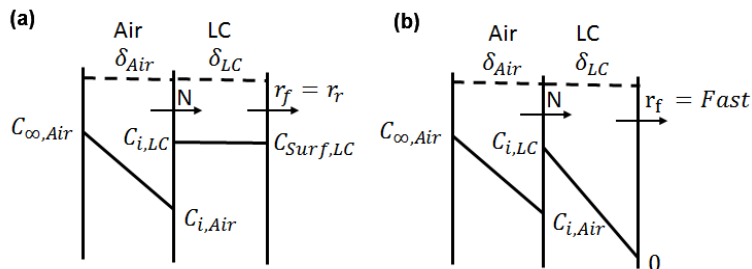


Figure S8. Schematic illustration of the concentration profile of the analyte with flux N as it diffuses from the air ($C_{\infty,\text{Air}}$) to the surface. (a) Equilibrated surface model described by Hunter and Abbott with constant concentration of the analyte in the LC film assuming that the forward reaction rate (r_f) is equal to the reverse reaction rate (r_r).¹⁸ (b) Fast reaction model for O_3 and Cl_2 detection with zero concentration of the analyte in the LC near the surface. The analyte diffuses through two regimes in both cases: (1) vapor phase concentration boundary layer with thickness δ_{Air} and (2) liquid crystal phase with thickness δ_{LC} . The concentration on the air side of the air-LC interface is defined as $C_{i,\text{Air}}$ and the concentration on the LC side ($C_{i,\text{LC}}$) is defined as $\frac{C_{i,\text{Air}}}{H}$, related by Henry's law coefficient (H).

This model does not describe the dynamic LC response to O_3 reported in this paper, specifically that the response dynamics are independent of the identity of the metal cations on the surface. However, a modification of the model in which the reaction is assumed to be sufficiently fast to deplete the concentration of reactant at the solid-LC interface does agree with experimental trends. We call this modification the “fast reaction model”. To derive the “fast reaction model” equation, we first start by defining the flux of the analyte across the air (N_{Air}) and LC phase (N_{LC}) in Equation S4 and Equation S5, respectively, assuming Fick's law of diffusion.

$$N_{\text{Air}} = \frac{-D_{\text{Air}}}{\delta_{\text{Air}}} (C_{i,\text{Air}} - C_{\infty,\text{Air}}) \quad \text{S4}$$

$$N_{LC} = \frac{-D_{LC}}{\delta_{LC}} \left(C_{i,Surface} - \frac{C_{i,Air}}{H} \right) \quad S5$$

The flux on the air side depends on the diffusion constant of the analyte in air (D_{Air}), concentration boundary layer thickness (δ_{Air}), and the concentration of the analyte at both boundaries, as defined in Figure S8b. D_{Air} is estimated to be 0.30 cm²/s for O₃³⁰ and 0.13 cm²/s for Cl₂, as estimated by using Equation S13; vide infra.³¹ Similarly, the flux on the LC side is dependent on the diffusion constant of the analyte in the LC (D_{LC}), LC thickness (δ_{LC}), and the concentration of the analyte at the surface ($C_{i,Surface}$) and at the LC-air interface ($C_{i,LC} = \frac{C_{i,Air}}{H}$). It is assumed that the analyte on the LC-side and the air-side of the LC-air interface is in equilibrium; thus, the two concentrations are correlated via the Henry's law coefficient (H). In order to approximate the Henry's law coefficient of O₃ and Cl₂ at the air-LC interface, we refer to the study of Sheavly *et al.* which used an all-atom force field molecular dynamics (MD) simulation to model partition and diffusion of O₃ and Cl₂ in 5CB. The calculated Henry's law coefficient of O₃ and Cl₂ from MD simulations is 0.0127 and 0.2365 cG/cL, respectively.³² The diffusion constants of O₃ and Cl₂ in the LC phase predicted by the MD simulations of Sheavly *et al.* (along the director) are 375.55 μm²/s and 243.89 μm²/s for O₃ and Cl₂, respectively.

If we assume pseudo-steady concentration profiles, then the flux (N) of the analyte in the air and LC phase must be equal as described in Equation S6. We can combine Equation S4-6 to derive Equation S7.

$$N = N_{Air} = N_{LC} \quad S6$$

$$N = S_A \frac{d\theta_i}{dt} = \frac{1}{\left(\frac{\delta_{Air}}{D_{Air}} + \frac{H\delta_{LC}}{D_{LC}} \right)} \left(C_{\infty,Air} - H C_{i,Surface} \right) \quad S7$$

In Equation S7, we define the flux as being equal to the derivative of the fraction of surface sites covered by the analyte (θ_i) with respect to time multiplied by the surface density of sites (S_A). We estimate S_A from a DFT derived lattice constant for metal salts (see above). Solving Equation S7, requires knowledge of the rate expression of the surface reaction because the concentration of the analyte at the surface ($C_{i,Surface}$) depends on this rate expression, which will also depend on the fraction of sites covered by the analyte (θ_i). To simplify this derivative and solve this expression analytically, we assume a fast reaction and constrain $C_{i,Surface}$ to zero (see in Figure S8b). With this assumption, we derive Equation S8,

$$\frac{d\theta_i}{dt} = \frac{C_{\infty,Air}}{S_A \left(\frac{\delta_{Air}}{D_{Air}} + \frac{H\delta_{LC}}{D_{LC}} \right)} = \frac{C_{\infty,Air} K_G}{S_A} \quad S8$$

where K_G is defined as the overall mass transfer coefficient. Note that the right-hand side of Equation S8 is now independent of θ_i and t. We can integrate this expression (Equation S9) and derive Equation S10 where the time (t_R) defines when some threshold of analyte is reached on the surface (θ_{thresh}).

$$\int_0^{\theta_{i,thresh}} d\theta_i = \frac{C_{\infty,Air} K_G}{S_A} \int_0^{t_R} dt \quad S9$$

$$t_R = \frac{S_A \theta_{thresh}}{K_G C_{\infty,Air}} \quad S10$$

The resulting Equation S10 is only part of the total transport time. For $t_{transport}$, we also include the advection time (t_{adv}) for the analyte to travel from the gas cylinder to the LC cell, and the characteristic time (t_{char}) required for diffusion of the analyte from the vapor phase to the solid surface, which is estimated by equation S11.¹⁸ We also include t_{add} , a time shift for providing a best fit with experimental data.

$$t_{transport} = t_R + t_{char} = t_R + \frac{\delta_{Air}^2}{2D_{Air}} + \frac{\delta_{LC}^2}{2D_{LC}} + t_{adv} + t_{add} \quad S11$$

2. Calculation of transport parameters

The calculation of the diffusion length in the vapor phase is discussed next. As shown in Figure S9, the gas stream flows parallel to the LC film within the flow cell. The total volume of the flow cell was 18 cm³ (5 cm x 4.8 cm x 0.8 cm), giving rise to a residence time of 1.8 seconds when the flow rate was 600 mL/min. The Reynolds number was calculated to be 26 for flow within the flow cell at 600 mL/min. This value corresponds to laminar flow. The flow of the gas stream across the glass substrate leads to the development of a hydrodynamic boundary layer with a thickness δ that can be evaluated for laminar flows. The concentration boundary layer thickness in the gas phase, δ_{Air} (in cm), was calculated using Equation S12, which was developed for mass transfer over flat plates in laminar flow.³³ The value of δ_{Air} is calculated to be 1.18 cm for O₃ and 0.89 cm for Cl₂ using Equation S12:

$$\delta_{Air} = 3.0 \left(\frac{x}{U_{\infty}} \right)^{\frac{1}{2}} \left(1 - \left(\frac{x_0}{x} \right)^{\frac{3}{4}} \right)^{\frac{1}{3}} (v_G)^{\frac{1}{6}} (D_{Air})^{\frac{1}{3}} \quad S12$$

The value of x is 2 cm, which represents the horizontal distance from the edge of substrate glass to the center of the TEM grid, and x_0 (0.15 cm) is the horizontal distance from the edge of TEM grid to the center of the TEM grid (Figure S9). U_∞ is the velocity of the gas stream, which is 0.0278 m/s for the gas volumetric flow of $F=600$ mL/s. We calculate the gas velocity from the cross-sectional area (A) $U_\infty=F/A$. The cross-sectional area of the cell is $A=4.5 \times 0.8$ cm². ν_G is the kinematic viscosity of air, which is 14.8 cSt at 15°C. The diffusivity of the analyte in air (D_{air}) is calculated using Equation S13 using the Fuller, Schettler, Giddings Method (D_{AB} refers to diffusion of gas species A in gas species B).³¹

$$D_{AB} = \frac{10^{-3} T^{1.75} \left(\frac{1}{M_A} + \frac{1}{M_B} \right)^{\frac{1}{2}}}{P \left[(\Sigma V_A)^{\frac{1}{3}} + (\Sigma V_B)^{\frac{1}{3}} \right]^2} \quad \text{S13}$$

where V_A is the special diffusion parameter to be summed over atoms, groups, and structures for compound A and B. For O₃ and Cl₂ diffusion in air, $\Sigma V_{O_3} = 16.48$, $\Sigma V_{Cl_2} = 39$, and $\Sigma V_{Air} = 20.1$ cm³/(g·mol). The total pressure (P) is 1 atm. The temperature T is 300 K. M_A and M_B are the molecular weight for compound A and B. For O₃ and Cl₂ diffusion in air, $M_{O_3} = 48$, $M_{Cl_2} = 70.91$, and $M_{Air} = 28.96$ g/mol. The values of diffusivity calculated from Equation S13 are: $D_{O_3,air} = 0.18 \frac{cm^2}{s}$ and $D_{Cl_2,air} = 0.13 \frac{cm^2}{s}$. In the manuscript, we only use the Cl₂ value calculated using Equation S13. We used an experimentally determined value for the diffusivity of O₃ in air in the manuscript ($0.30 \frac{cm^2}{s}$),³⁰

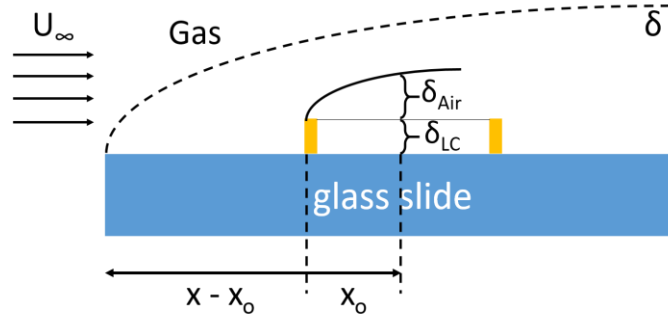


Figure S9. A schematic illustration of the boundary layer thickness (hydrodynamic and concentration) that determine mass transfer of O₃ and Cl₂ to the metal salts-decorated surface that supports the film of LC. The hydrodynamic boundary layer thickness is indicated by δ and the concentration boundary layer by δ_{Air} . Other parameters shown in the figure are defined in the text.

3. Parameter Fitting with Reaction-Diffusion Model

We have one unknown variable in Equation S10, which is the threshold fraction of oxidized sites that generates a LC response (θ_{thresh}). We assume that θ_{thresh} is the same for O₃ and Cl₂ detection. The best fit value of θ_{thresh} was found to be 38% of Mn(ClO₄)₂ sites, a value that was used in Figure 8 and Figure S10 for both O₃ and Cl₂.

The overall mass transfer coefficient (K_G) in Equation S10 is evaluated as

$$K_G = \frac{1}{k_{air} + k_{LC}} = \frac{1}{\frac{\delta_{Air}}{D_{air}} + \frac{H\delta_{LC}}{D_{LC}}} \quad \text{(S14)}$$

where k_{air} and k_{LC} are the mass transfer coefficients for the vapor phase and LC, respectively, evaluated as

$$k_{air} = \frac{\delta_{Air}}{D_{air}} \quad \text{(S15)}$$

$$k_{LC} = \frac{H\delta_{LC}}{D_{LC}} \quad \text{(S16)}$$

We optimized the values of k_{LC} because this term contains the MD-calculated values of D_{LC} and H . By increasing k_{LC} of O₃ by a factor of 1.59 and decreasing k_{LC} of Cl₂ by a factor 1.59 (Table S6), we were able to obtain better agreement between experimental data and the model (Figure 8 or also shown in Figure S10a b). We show the fit if we do not make any changes to k_{LC} in Figure S10e for O₃ and Figure S10f for Cl₂.

Table S6. Comparison of the mass transfer coefficients for the vapor phase k_{air} (Equation S15) and the LC phase k_{LC} (Equation S16) using data³² and values of k_{LC} obtained by fitting the model in Figure 8 to the data in Figure 7.

Analyte	k_{air} (s/cm)	k_{LC} (s/cm)	Fit value of k_{LC} (s/cm)
O ₃	3.9	6.1	9.7
Cl ₂	6.9	175	110

Inspection of Table S6 reveals that for O₃, k_{air} (3.9 s/cm) and k_{LC} (6.1 s/cm) are estimated from prior molecular dynamics simulations to be similar in order of magnitude, which suggests that O₃ diffusion is impacted by the vapor phase concentration boundary layer thickness and the LC thickness. However, the value of k_{LC} obtained from fitting our model to the experimental response times (9.7 s/cm) suggests that diffusion of O₃ across the LC film is the dominant rate-limiting process. For the case of Cl₂, we find that the value of k_{LC} (ranging from 175 s/cm or 110 s/cm) is much larger than k_{air} (6.9 s/cm) leading us to also conclude that the Cl₂ response is rate-limited by diffusion on the LC side. These results suggest that the rate-limiting step of the LC response to these analytes differs from the previously studied case of DMMP detection on Al(ClO₄)₃, where it was found that diffusion was limited on the air side. This difference arises because the Henry's law coefficient (H) of DMMP between gas and 5CB is $\sim 5.3 \times 10^{-5}$.¹⁸ This is three orders of magnitude smaller than the value for O₃ (0.013) or four orders of magnitude smaller than the value used for Cl₂ (0.24). These large changes in the Henry's law coefficient directly influence Equation S14, which changes the rate limiting process.

By fitting this model to the experimental data for O₃, we find $t_{add} = 10$ seconds provides a best fit (Figure 8 and Figure S10a b). The experimental response time for O₃ (Figure 8 and Figure S10a) is defined as the time required to reach 10% normalized light intensity (Figure 7). We report how the model predictions in Figure 8 and Figure S10a change if we set t_{add} equal to zero (Figure S10c). The physical origin of the t_{add} term is unknown, but it likely reflects the decomposition of O₃ prior to reaching the metal salt-decorated surface. In water, ozone generally decomposes rapidly.³⁴ We hypothesize that a similar effect may happen here where during the first 10 seconds ozone undergoes decomposition. In Figure S10a, we report the best fit model for O₃ that used a t_{add} of 10 seconds, and we can compare this model to Figure S10c, which used $t_{add} = 0$ second. In Figure S10c, it is clear that the first two points (100 ppm and 1290 ppm) do not match the model curve. It was not possible to match these points by changing the diffusion coefficients or Henry's law coefficient. We do not included the 10 seconds t_{add} for Cl₂ in Figure 8c because the rate of decomposition of Cl₂ is expected to be slower than O₃. However, by comparing Figure S10b, Cl₂ modeled with $t_{add} = 10$ seconds and Figure S10d, modeled without t_{add} , we note that inclusion or omission of $t_{add} = 10$ seconds has little impact on the level of agreement between the model and experimental observation.

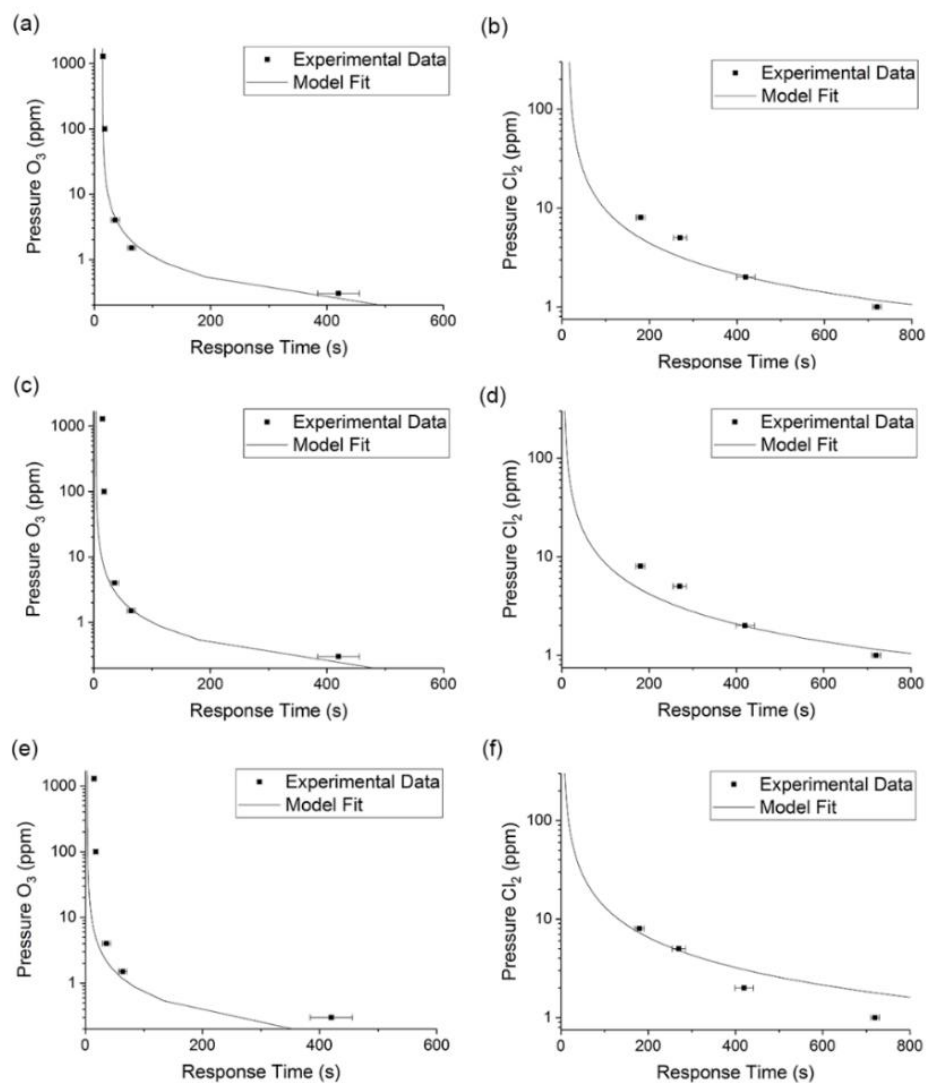


Figure S10. Comparison of experimental data to the fast reaction model prediction for different values of t_{add} and k_{LC} . All experimental data was collected using 15 ± 3 pmol/mm² Mn(ClO₄)₂ exposed to humid O₃ (a, c, and e) at 1290 ± 40 , 100 ± 10 , 4 ± 1 , 1.5 ± 0.2 , and 0.3 ± 0.1 ppm or exposed to humid Cl₂ (b, d, and f) at 8 ± 0.3 , 5 ± 0.2 , 2 ± 0.1 , and 1 ± 0.1 ppm; humidity is always kept at 20% RH. (a) and (b) shows the model prediction with a t_{add} of 10 second and the best fit values of k_{LC} described in Table S6 for O₃ and Cl₂, respectively. (c) and (d) shows model predictions with a t_{add} of 0 second and the best fit values of k_{LC} described in Table S6 for O₃ and Cl₂, respectively. (e) and (f) shows model predictions with t_{add} of 10 second and best fit k_{LC} values.

References

- 1 J. L. Pascal, J. Potier, D. J. Jones, J. Roziere and A. Michalowicz, *Inorg. Chem.*, 1985, **24**, 238–241.
- 2 W. H. Baur, *Acta Crystallogr. Sect. B Struct. Crystallogr. Cryst. Chem.*, 1976, **32**, 2200–2204.
- 3 M. Casas-Cabanas, J. Canales-Vazquez, J. Rodriguez-Carvaja and M. Rosa Palacín, *Mater. Res. Soc. Symp. Proc.*, 2009, **1126**, 1126.
- 4 NIST Inorganic Crystal Structure Database, NIST Standard Reference Database Number 3. National Institute of

Standards and Technology: Gaithersburg MD, 20899.

- 5 G. A. E. Oxford and A. M. Chaka, *J. Phys. Chem. C*, 2012, **116**, 11589–11605.
- 6 J. Neugebauer and M. Scheffler, *Phys. Rev. B*, 1992, **46**, 16067–16080.
- 7 J. I. Gold, T. Szilvási, N. L. Abbott and M. Mavrikakis, *ACS Appl. Mater. Interfaces*, 2020, **12**, 30941–30953.
- 8 T. Szilvási, L. T. Roling, H. Yu, P. Rai, S. Choi, R. J. Twieg, M. Mavrikakis and N. L. Abbott, *Chem. Mater.*, 2017, **29**, 3563–3571.
- 9 T. Szilvási, N. Bao, H. Yu, R. J. Twieg, M. Mavrikakis and N. L. Abbott, *Soft Matter*, 2018, **14**, 797–805.
- 10 H. Yu, T. Szilvási, P. Rai, R. J. Twieg, M. Mavrikakis and N. L. Abbott, *Adv. Funct. Mater.*, 2018, **28**, 1703581.
- 11 M. Deborde and U. von Gunten, *Water Res.*, 2008, **42**, 13–51.
- 12 S. Allard, L. Fouche, J. Dick, A. Heitz and U. Von Gunten, *Environ. Sci. Technol.*, 2013, **47**, 8716–8723.
- 13 J. Wang, M. R. Voss, H. Busse and B. E. Koel, 1998, **5647**, 4693–4696.
- 14 R. Sander, *Atmos. Chem. Phys.*, 2015, **15**, 4399–4981.
- 15 U. J. Jáuregui-Haza, E. J. Pardillo-Fontdevila, A. M. Wilhelm and H. Delmas, *Lat. Am. Appl. Res.*, 2004, **34**, 71–74.
- 16 K. Rakness, G. Gordon, B. Langlais, W. Masschelein, N. Matsumoto, Y. Richard, C. M. Robson and I. Somiya, *Ozone Sci. Eng.*, 1996, **18**, 209–229.
- 17 R. Triandi Tjahjanto, D. Galuh R. and S. Wardhani, *J. Pure Appl. Chem. Res.*, 2012, **1**, 18–25.
- 18 J. T. Hunter and N. L. Abbott, *Sensors Actuators, B Chem.*, 2013, **183**, 71–80.
- 19 P. D. T. Huibers and D. O. Shah, *Langmuir*, 1997, **13**, 5995–5998.
- 20 N. A. Lockwood, J. K. Gupta and N. L. Abbott, *Surf. Sci. Rep.*, 2008, **63**, 255–293.
- 21 F. Bardé, M. R. Palacin, B. Beaudoin, A. Delahaye-Vidal and J. M. Tarascon, *Chem. Mater.*, 2004, **16**, 299–306.
- 22 Y. C. Liu, J. A. Koza and J. A. Switzer, *Electrochim. Acta*, 2014, **140**, 359–365.
- 23 Y. Chen, J. Zhou, P. Maguire, R. O’Connell, W. Schmitt, Y. Li, Z. Yan, Y. Zhang and H. Zhang, *Sci. Rep.*, 2016, **6**, 1–8.
- 24 A. Kudielka, S. Bette, R. E. Dinnebier, M. Abeykoon, C. Pietzonka and B. Harbrecht, *J. Mater. Chem. C*, 2017, **5**, 2899–2909.
- 25 L. Tian, J. L. Zhu, L. Chen, B. An, Q. Q. Liu and K. L. Huang, *J. Nanoparticle Res.*, 2011, **13**, 3483–3488.
- 26 Y. SUN, J. PAN, P. WAN, C. XU and X. LIU, *Chinese J. Chem. Eng.*, 2007, **15**, 262–267.
- 27 M. Casas-Cabanas, J. Canales-Vázquez, J. Rodríguez-Carvajal and M. R. Palacín, *J. Am. Chem. Soc.*, 2007, **129**, 5840–5842.
- 28 Y. Li, C. He, E. V. Timofeeva, Y. Ding, J. Parrondo, C. Segre and V. Ramani, *Front. Energy*, 2017, **11**, 401–409.
- 29 F. Bardé, M. R. Palacín, B. Beaudoin and J. M. Tarascon, *Chem. Mater.*, 2005, **17**, 470–476.
- 30 F. Hegeler and H. Akiyama, *Dig. Tech. Pap. Int. Pulsed Power Conf.*, 1997, **2**, 1085–1090.
- 31 E. N. Fuller, P. D. Schettler and J. C. Giddings, *Ind. Eng. Chem.*, 1966, **58**, 18–27.
- 32 J. K. Sheavly, J. I. Gold, M. Mavrikakis and R. C. Van Lehn, *Mol. Syst. Des. Eng.*, 2020, **5**, 304–316.
- 33 J. Krenn, S. Baesch, B. Schmidt-Hansberg, M. Baunach, P. Scharfer and W. Schabel, *Chem. Eng. Process. Process Intensif.*, 2011, **50**, 503–508.
- 34 J. HOIGNÉ and H. Bader, *Ozone Sci. Eng.*, 1994, **16**, 121–134.